Communication

In Situ Observation of the Nucleation and Growth of Ferrite Laths in the Heat-Affected Zone of EH36-Mg Shipbuilding Steel Subjected to Different Heat Inputs

XIAODONG ZOU, JINCHENG SUN, HIROYUKI MATSUURA, and CONG WANG

The nucleation and growth behaviors of ferrite laths in the heat-affected zone (HAZ) of EH36-Mg shipbuilding steel with different heat inputs were observed *in situ* by high-temperature confocal scanning laser microscope (CSLM). It was found that ferrite laths prefer to nucleate on the surface of inclusions instead of grain boundaries under the heat input of 120 kJ/cm, while FSPs are easier to form in 210 kJ/cm due to a significantly reduced cooling rate.

https://doi.org/10.1007/s11663-018-1326-4

To improve the cruising range of ships and to reduce the building costs, shipbuilding steels are required to carry superior properties such as high strength, outstanding toughness, and excellent weldability. One proven way of enhancing shipbuilding efficiency and reducing cost is to implement high heat input welding during manufacturing *via* demonstrated techniques such as submerged arc welding and electroslag welding.[1,2] However, high heat input welding usually leads to significant coarsening of austenite grains and formation of microstructures, such as ferrite side plate (FSP) and upper bainite, which invariably lead to the reduced toughness of the heat-affected zone (HAZ).[3–5]

Intragranular acicular ferrite (AF) is regarded as the optimal microstructure combining excellent strength and toughness.[6,7] This is due to the fact that AFs, generally nucleating on the potent nonmetallic inclusions in the prior austenite grain, carry chaotic arrangements of laths and fine-grained interlocking microstructure features that effectively divide prior austenite grain into several subgrains and inhibit the propagation of cracks.[8,9] Therefore, AF nucleation on inclusions within coarse austenite grains is a solution to improve the toughness of HAZ for shipbuilding steels.[10,11]

It is found that the nucleation of AF is affected by several factors such as the characteristics of inclusions and cooling rate during solidification.[8,9,11–15] Xu *et al.*[11] reported that Mg-containing inclusions could effectively facilitate the nucleation of AF and improve the toughness of HAZ in EH36 shipbuilding steel, and the fraction of AF increased with the increase of Mg content from 0 to 99 ppm. Yang *et al.*[15] found that there was an optimal cooling rate for the formation of AF in the medium-carbon steel with 0.025 pct Ti. Sung *et al.*[16] suggested that the volume fraction of AF in HAZ of API X80 pipeline steels decreased as the heat input increased from 35 to 60 kJ/cm due to decreasing cooling rate during $\gamma \rightarrow \alpha$ transformation. Hence, correlation studies involving formation of AF and welding heat input are necessary to derive appropriate welding conditions and microstructures.

A high-temperature confocal scanning laser microscope (CSLM) enables observation of the nucleation and growth of AF during welding *in situ*.[17–19] The present work aims to investigate the effect of welding heat input on the microstructure in the HAZ of EH36-Mg shipbuilding steel. Concurrent to *in situ* observation of AF nucleation and growth by CSLM, crystallographic orientations of microstructural features in HAZ are performed by electron backscatter diffraction (EBSD) to offer quantitative explanations.

Chemical compositions of the targeted steel, namely, EH36-Mg, are shown in the Table I. Detailed manufacturing processes are presented in the previous work.[20] To simulate welding, samples with a size of 11 × 11 × 80 mm were prepared for HAZ simulation on a Gleeble 1500D machine. The simulated peak temperature was set at 1573 K with a dwell time of 3 seconds. Targeted heat inputs were estimated to be 120 and 210 kJ/cm corresponding to the cooling times from 1073 K to 773 K of 196 and 596 seconds, respectively. Thermal cycles were described by employing the Rykalin-2D heat-transfer model.

All specimens after welding thermal simulation were prepared in the sequence of cutting, grinding, polishing, and etching in a 4 pct nital solution. Microstructures were observed by a field emission–scanning electron microscope (FE-SEM, model: Hitachi SU8010) with an energy-dispersive spectrometer. The crystallographic orientations were analyzed using a FE-SEM (JSM-7800F, JEOL*) operating at 20.0 kV combined

XIAODONG ZOU, JINCHENG SUN, and CONG WANG are with the School of Metallurgy, Northeastern University, Shenyang 110819, China. Contact email: wangc@smm.neu.edu.cn HIROYUKI MATSUURA is with the Department of Materials Engineering, The University of Tokyo, Tokyo 113-8656, Japan.

Manuscript submitted May 3, 2018.
Article published online July 16, 2018.

*JEOL is a trademark of Japan Electron Optics Ltd., Tokyo.

Table I. Chemical Composition of the EH36-Mg Steel Plate (Weight Percent)

Steel	C	Si	Mn	Ni	Al	B	Ti	V	Nb	O	N	Mg	S
EH36-Mg	0.052	0.15	1.53	0.36	0.0065	0.0008	0.01	0.014	0.014	0.0019	0.0027	0.0007	0.004

with an EBSD system (NordlysNano, Oxford Instruments) with a step size of 0.23 μm and HKL CHANNEL5 software.

Cylindrical specimens with a size of 5 mm in diameter and 3.5 mm in height from the steel were also machined. After polishing, they were heat treated under high-purity Ar after vacuuming up to 0.1 Pa in the furnace of a CSLM (VL2000DX-SVF17SP). Specimens were heated to 1473 K at 5 K/s and held for 60 seconds. They were subsequently cooled to 773 K, and the cooling time from 1073 K to 773 K was controlled to be 196 and 596 seconds at the cooling rate of 92 and 30 K/min, corresponding to the $t_{8/5}$ of 120 and 210 kJ/cm, respectively. It is worth noting that the cooling durations from 1473 K to 773 K are consistent with the corresponding cooling rate in welding thermal simulation to achieve heat input variations. For convenience, the specimens are referred to as "E120" and "E210," referring to heat input of 120 and 210 kJ/cm, respectively. During cooling, photographs were taken at a speed of five images per second by a charge-coupled-device camera. The ferrite lath's lengthening rate was determined from the slope of the length *vs* time plot.

Figure 1 shows the typical transformation of ferrite *in situ* at E120. It can be seen that the first lath-shaped ferrite preferentially nucleates on an inclusion at 975.2 K (Figure 1(a)), which is considered as AF. Subsequently, the second intragranular ferrite lath nucleates at 973.6 K (Figure 1(b)). At 957.3 K, the lengthening of the two ferrite laths stops by impinging on a subgrain boundary (Figure 1(c)). Then, the third ferrite lath forms from grain boundaries and grows into the matrix at 954.1 K (Figure 1(d)), which is considered as FSP. However, its lengthening process is stopped on the boundary of the other side of the matrix at 949.5 K (Figure 1(e)). After that, the fourth intragranular ferrite lath begins to nucleate at 941.7 K and stops at 936.6 K (Figures 1(f) and (g)). It is well known that the energy barrier for ferrite nucleation on the surface of inclusions is generally higher than that on a prior austenite grain boundary.[21] Therefore, ferrites are expected to preferentially nucleate on the grain boundaries rather than on the surfaces of inclusions. In the study, inclusions become the favorite nucleation sites for ferrites, which suggests the energy barrier of the inclusions is dwarfed. Ferrite length was correlated with cooling time for the four ferrite laths, as shown in Figure 1(h). It is found that ferrite lath length approximately follows a linear relationship with respect to cooling time. The lengthening rates of the three AFs (the first, second, and fourth lath) are 2.0, 4.3, and 3.5 μm/s, respectively, and that of the FSP (the third lath) is 4.4 μm/s. Although the nucleation sites for AF and FSP are different, the lengthening rates are similar. Actually, the rate will vary with temperature.[22]

Figure 2 shows the nucleation and growth of ferrite laths in E210. It can be seen that the first ferrite lath nucleates on the austenite grain boundary and grows into the grain at 1003.3 K (Figure 2(a)), which is followed by an intragranular ferrite lath nucleation at 993.1 K (Figure 2(b)). Subsequently, another two ferrite laths nucleate on the grain boundary at 986.7 K (Figure 2(c)). At 963.9 K, the ferrite laths stop growing (Figure 2(d)). Their lengthening rates are 1.4, 2.5, and 0.9 μm/s, respectively, which are slightly lower than those of E120. The lengthening rate of ferrite lath depends on the $\gamma \rightarrow \alpha$ transformation temperature, namely, the higher the temperature is, the smaller is the driving force.[22] The ferrite formation temperature (1003.3 K, as shown in Figure 2(a)) in E210 is higher than that (975.2 K, as shown in Figure 1(a)) in E120, leading to a lower lengthening rate.

Figures 3(a) and (b) shows typical SEM micrographs for E120 and E210 after welding thermal simulation, respectively. Outstanding microstructures are marked in the micrographs. For E120, the microstructures are dominated by polygonal ferrites (PFs), pearlites, and AFs. It can be seen that the lath of AF nucleates and grows on an inclusion, which was recognized as an Al-Mg-Ti-O-(Mn-S) complex inclusion in the previous study.[23] As the ferrite first forms at high temperature, the transformed austenite is gradually rejected with C and pearlite forms due to local high C content.[24] For E210, the area fraction of PF decreases and FSP forms, as shown in Figure 3(b). The microstructures of specimens after CSLM observation are similar to those after welding thermal simulation. Figures 3(c) through (e) show the orientation image maps and corresponding misorientation angle distribution histograms of E120 and E210, respectively. In E120, the microstructure in the orientation image map is mainly coarse ferrite. In E210, more pearlite is formed, which is usually the crack source and contributes to a crack initiation energy and crack propagation energy decrease.[24] In the orientation image maps, misorientation boundaries of 2 to 15 deg and $\geq$ 15 deg are defined as low-angle and high-angle grain boundaries, respectively. The distribution of the misorientation angle shows a bimodal character in both E120 and E210 with peaks at low and high angles, as shown in Figure 3(e). Various reports demonstrated that the bimodal grain microstructure can facilitate high strength and ductility of metallic materials, where such nonequilibrium grain boundaries provide a high density of dislocations for slip and can even render grains to slide or rotate.[25–28] In addition, the frequency of high-angle grain boundaries in E120 is slightly higher than that in E210, which can deflect or even hinder the propagation of cleavage cracks.[29]

Based on the observations demonstrated in Figures 1 and 2, it is clear that the starting temperatures of FSP

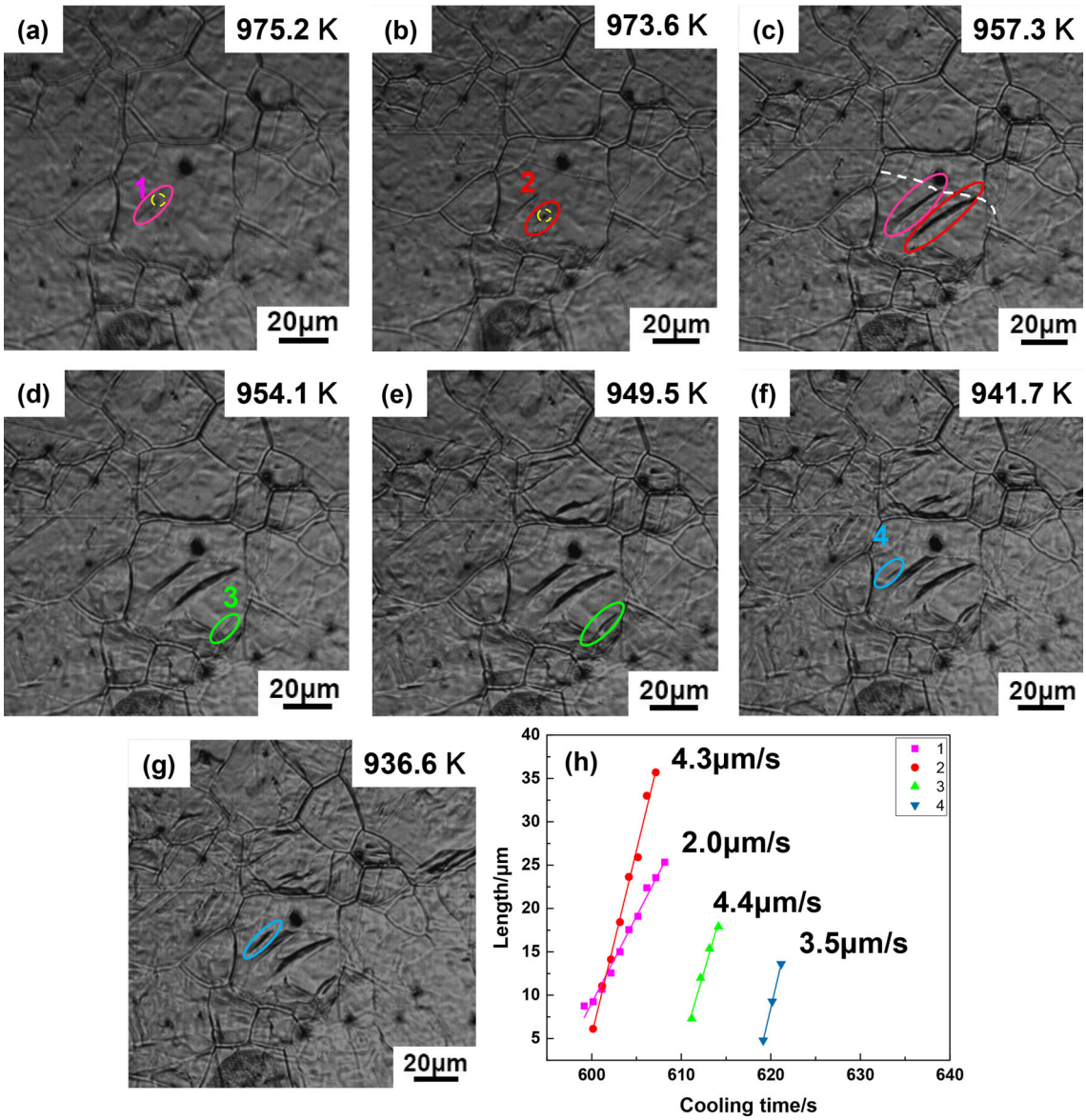

Fig. 1—(*a* through *g*) CSLM snapshots of nucleation and growth of four salient ferrite laths and (*h*) the relationship between growing ferrite length against cooling time for the four ferrite laths at E120 (1: the first ferrite lath, 2: the second ferrite lath, 3: the third ferrite lath, 4: the fourth ferrite lath, yellow circle: inclusion, and white dashed line: subgrain boundary) (Color figure online).

and AF ($T_{FSP,s}$ and $T_{AF,s}$) decrease with increasing cooling rate. The values of $T_{FSP,s}$ and $T_{AF,s}$ for E120 and E210 are chosen to constitute a schematic continuous cooling transformation (CCT) diagram, as shown in Figure 4. It is found that $T_{AF,s}$ is higher than $T_{FSP,s}$ in E120, while $T_{AF,s}$ is lower than $T_{FSP,s}$ in E210, which is expected since the inclusions should be the primary nucleation sites under higher cooling rate and grain boundaries become the preferential nucleation sites under lower cooling rate. Connecting $T_{FSP,s}$ and $T_{AF,s}$ in E120 and E210 will lead to an intersection (813.6 seconds, 986.7 K) marked by the red square shown in Figure 4. It is suggested that there is a critical cooling rate between 30 and 92 K/min that renders $T_{AF,s}$ equal to $T_{FSP,s}$, as indicated by the dashed blue lines. When the cooling rate is higher than the critical value, as in the shaded area, effective inclusions could be the primary nucleation sites; however, when the cooling rate is lower than the critical value, ferrite laths prefer to form on grain boundaries.

During continuous cooling, the undercooling degree is one of the important factors governing the growth behavior of ferrite.[30] It is further known that the formation of side-plate microstructure requires a relatively smaller driving force to break through the energy barrier and can occur at higher temperatures with smaller undercooling.[31] The formation of AF, on the other hand, requires a greater degree of undercooling and occurs at lower transformation temperatures. Hence, the FSP structures will be more preferentially formed than AF in E210 due to lower undercooling. However, in order to promote the nucleation of AF, increasing the energy barrier on grain boundaries and reducing that on the surface of inclusions is imperative.

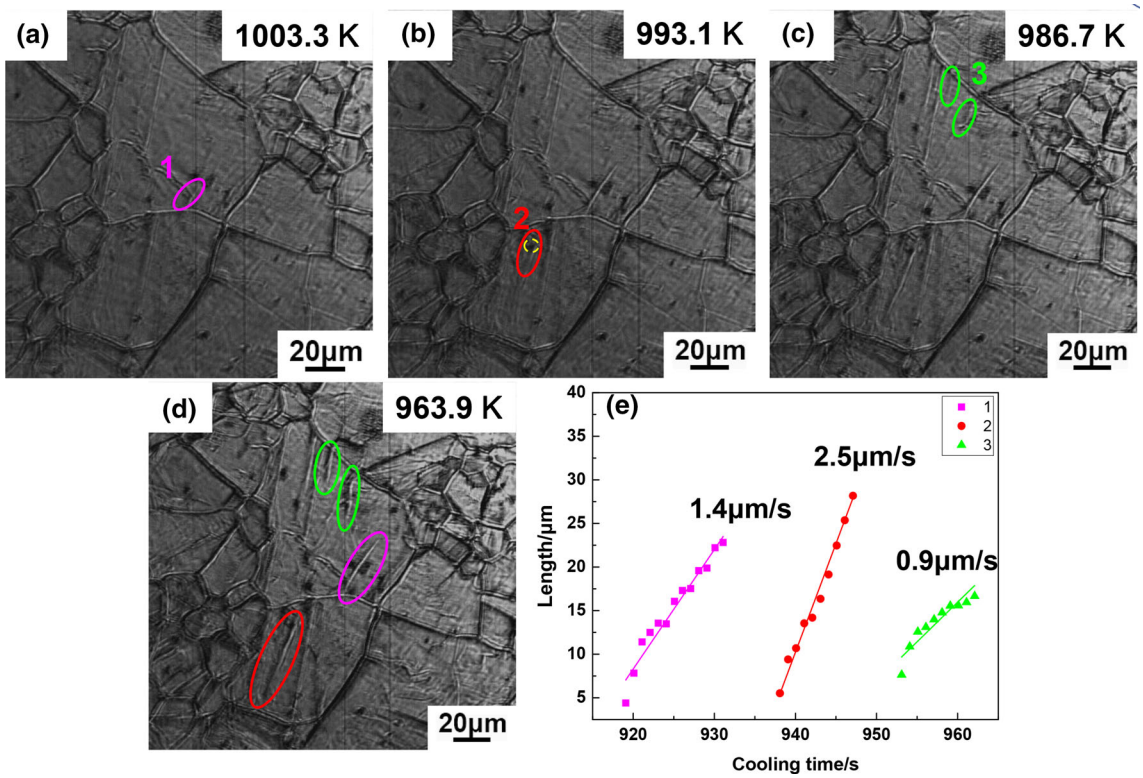

Fig. 2—(*a* through *d*) CSLM snapshots of nucleation and growth of four salient ferrite laths and (*e*) the relationship between growing ferrite length against cooling time for the four ferrite laths at E210 (1: the first ferrite lath, 2: the second ferrite lath, 3: the third and fourth ferrite laths, and yellow circle: inclusion) (Color figure online).

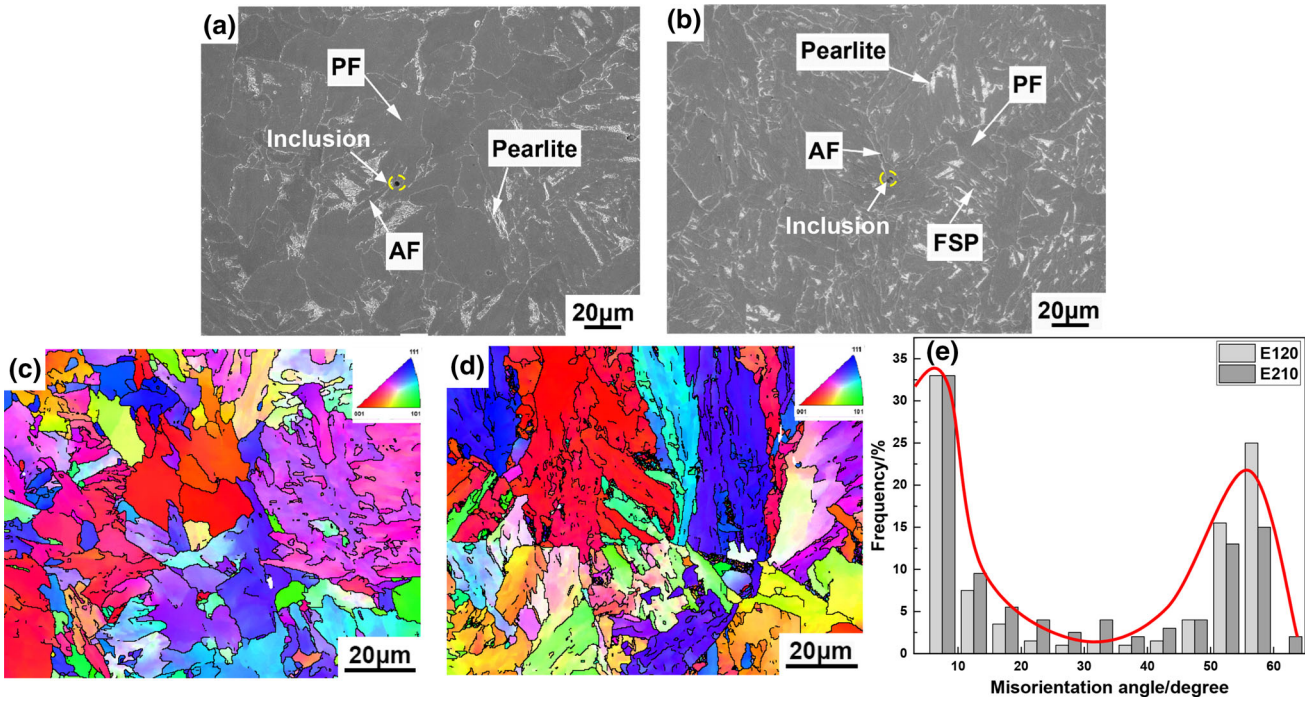

Fig. 3—SEM micrographs of the (*a*) E120 and (*b*) E210 specimens, orientation image maps of (*c*) E120 and (*d*) E210, and (*e*) misorientation angle distribution histograms for E120 and E210.

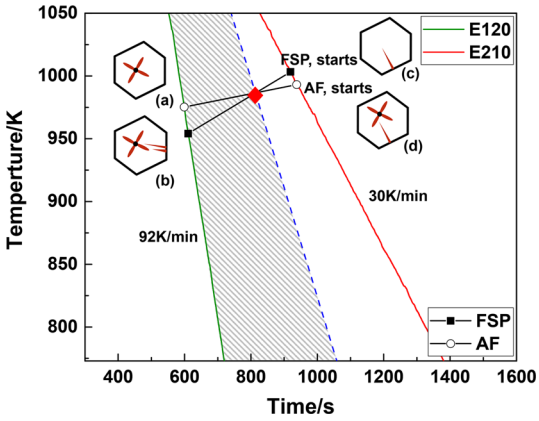

Fig. 4—Schematic CCT diagram for starting temperature of FSP and AF formation in E120 and E210.

The competition of ferrite nucleation between the grain boundaries and the inclusions is considerably affected by the characteristics of inclusions, the cooling rate, and the austenite grain size.[9,21,32,33] It was proven that the Al-Mg-Ti-O-(Mn-S) complex inclusions in the E120 and E210 can induce the nucleation of AF by absorbing Mn atom to form the Mn solute-depleted zone in the vicinity of inclusions and, thus, increase the chemical driving force for the austenite-ferrite transformation.[34] In addition, the energy barrier to heterogeneous nucleation of ferrite on inclusions will decrease significantly with increasing inclusion size.[32] However, the value for inclusions with diameters larger than about 1 μm decreases only slightly with a further increase of the inclusion size.[21] Both of the average sizes of Al-Mg-Ti-O-(Mn-S) complex inclusions in E120 and E210 are over 2 μm,[23] making them effective for AF nucleation. In addition, it is indicated that the driving force for ferrite formation increases with increasing cooling rate.[32] Therefore, it is easier for ferrite nucleation on the surface of inclusions in E120 with a higher cooling rate to break through the energy barrier than in E210.

In summary, this study demonstrated the microstructure in HAZ and *in situ* observation of ferrite lath growth in EH36 shipbuilding steel with different heat inputs, and the following conclusions can be drawn.

1. At lower heat input (E120), the ferrite lath prefers to nucleate on the surface of inclusions instead of grain boundaries due to the suppressed grain boundary energy barrier and larger driving force for AF formation. At higher heat input, since the cooling rate decreases, the formation of FSP can occur at higher temperatures, which demands a smaller driving force. In addition, there is a critical cooling rate between 30 and 92 K/min that renders the potency of AF formation equal to FSP.
2. The microstructures in E120 after welding thermal simulation are composed of dominant PF and fewer pearlite and AF. For E210, the area fraction of PF decreases as FSP forms. EBSD results indicate that the distribution of misorientation angles shows a bimodal character in both E120 and E210 with peaks at low and high angles, potentially enhancing strength and toughness.

The authors are grateful to the National Natural Science Foundation of China (Grant Nos. 51622401 and 51628402), Newton Advanced Fellowship by the joint Fund of Royal Society in the UK and the National Natural Science Foundation of China (Grant No. RP12G0414 and 51861130361), National Key Research and Development Program of China (Grant No. 2016YFB0300602), and Global Talents Recruitment Program endowed by the Chinese Government for their financial support. We also thank the Key Laboratory of Nuclear Materials and Safety Assessment, Institute of Metal Research, Chinese Academy of Sciences (Grant No. 2015KF04), and State Key Laboratory of Advanced Welding and Joining, Harbin Institute of Technology (Grant No. AWJ-16-Z04).

REFERENCES

1. A. Kojima, K. Yoshii, T. Hada, O. Saeki, K. Ichikawa, Y. Yoshida, Y. Shimura, and K. Azuma: *Nippon Steel Tech. Rep.*, 2004, pp. 33–37.
2. M. Minagawa, K. Ishida, Y. Funatsu, and S. Imai: *Nippon Steel Tech. Rep.*, 2004, pp. 6–8.
3. C. Lee, H. Bhadeshia, and H.-C. Lee: *Mater. Sci. Eng. A*, 2003, vol. 360, pp. 249–57.
4. A. Kojima, A. Kiyose, R. Uemori, M. Minagawa, M. Hoshino, T. Nakashima, K. Ishida, and H. Yasui: *Nippon Steel Tech. Rep.*, 2004, pp. 2–5.
5. S. Suzuki, K. Ichimiya, and T. Akita: *JFE Tech. Rep.*, 2005, vol. 5, pp. 24–29.
6. J. Lee and Y. Pan: *Mater. Sci. Eng., A*, 1991, vol. 136, pp. 109–19.
7. S. Ogibayashi: *Nippon Steel Tech. Rep.*, 1994, pp. 70–76.
8. L. Cheng and K. Wu: *Acta Mater.*, 2009, vol. 57, pp. 3754–62.
9. J.S. Byun, J.H. Shim, Y.W. Cho, and D.N. Lee: *Acta Mater.*, 2003, vol. 51, pp. 1593–1606.
10. Y. Kang, S. Jeong, J. Kang, and C. Lee: *Metall. Mater. Trans. A*, 2016, vol. 47A, pp. 2842–54.
11. L. Xu, J. Yang, R. Wang, Y. Wang, and W. Wang: *Metall. Mater. Trans. A*, 2016, vol. 47A, pp. 3354–64.
12. T.K. Lee, H.J. Kim, B.Y. Kang, and S.K. Hwang: *ISIJ Int.*, 2000, vol. 40, pp. 1260–68.
13. J.H. Shim, Y.J. Oh, J.Y. Suh, Y.W. Cho, J.D. Shim, J.S. Byun, and D.N. Lee: *Acta Mater.*, 2001, vol. 49, pp. 2115–22.
14. N. Kikuchi, S. Nabeshima, Y. Kishimoto, Y. Ishiguro, and S. Sridhar: *ISIJ Int.*, 2009, vol. 49, pp. 1036–45.
15. Z. Yang, F. Wang, S. Wang, and B. Song: *Steel Res. Int.*, 2008, vol. 79, pp. 390–95.
16. H.K. Sung, S.Y. Shin, W. Cha, K. Oh, S. Lee, and N.J. Kim: *Mater. Sci. Eng. A*, 2011, vol. 528, pp. 3350–57.
17. G. Mao, R. Cao, X. Guo, Y. Jiang, and J. Chen: *Metall. Mater. Trans. A*, 2017, vol. 48A, pp. 1–16.
18. J. Hamada, M. Enomoto, T. Fujishiro, and T. Akatsuka: *Metall. Mater. Trans. A*, 2014, vol. 45A, pp. 3781–89.
19. Q. Wang, X. Zou, H. Matsuura, and C. Wang: *Metall. Mater. Trans. B*, 2018, vol. 49B, pp. 18–22.
20. X. Zou, D. Zhao, J. Sun, C. Wang, and H. Matsuura: *Metall. Mater. Trans. B*, 2018, vol. 49B, pp. 481–89.
21. R. Ricks, P. Howell, and G. Barritte: *J. Mater. Sci.*, 1982, vol. 17, pp. 732–40.
22. X. Wan, K. Wu, L. Cheng, and R. Wei: *ISIJ Int.*, 2015, vol. 55, pp. 679–85.

23. J. Sun, X. Zou, H. Matsuura, and C. Wang: *JOM*, 2018, vol. 70, pp. 946–50.
24. J. Hu, L. Du, J. Wang, and C. Gao: *Mater. Sci. Eng. A*, 2013, vol. 577, pp. 161–68.
25. M. Zha, H. Zhang, Z. Yu, X. Zhang, X. Meng, H. Wang, and Q. Jiang: *J. Mater. Sci. Technol.*, 2018, vol. 34, pp. 257–64.
26. E. Ma: *Scripta Mater.*, 2003, vol. 49, pp. 663–68.
27. A. Hasnaoui, H.V. Swygenhoven, and P.M. Derlet: *Acta Mater.*, 2002, vol. 50, pp. 3927–39.
28. A.P. Zhilyaev, B.K. Kim, G.V. Nurislamova, M.D. Baró, J.A. Szpunar, and T.G. Langdon: *Scripta Mater.*, 2002, vol. 46, pp. 575–80.
29. A. Lambert-Perlade, A.F. Gourgues, and A. Pineau: *Acta Mater.*, 2004, vol. 52, pp. 2337–48.
30. M. Militzer, R. Pandi, and E. Hawbolt: *Metall. Mater. Trans. A*, 1996, vol. 27A, pp. 1547–56.
31. V. Muthupandi, P.B. Srinivasan, S. Seshadri, and S. Sundaresan: *Mater. Sci. Eng., A*, 2003, vol. 358, pp. 9–16.
32. W. Mu, H. Shibata, P. Hedström, P.G. Jönsson, and K. Nakajima: *Metall. Mater. Trans. B*, 2016, vol. 47B, pp. 2133–47.
33. D. Zhang, H. Terasaki, and Y.I. Komizo: *Acta Mater.*, 2010, vol. 58, pp. 1369–78.
34. Y. Hou, W. Zheng, Z. Wu, G. Li, N. Moelans, M. Guo, and B.S. Khan: *Acta Mater.*, 2016, vol. 118, pp. 8–16.